19

Real-Time Heterodyne Interferometry with Correlation Image Sensor

Akira Kimachi
Department of Engineering Informatics, Osaka Electro-Communication University
Japan

1. Introduction

Optical heterodyne interfereometry (HI) (R. Dändliker, 1973; N.A. Massie, 1979) is an interferometric technique that employs two interfering beams of slightly different frequencies. Interference of these beams yields a time-varying sinusoidal intensity signal whose frequency equals the difference between the frequencies of the two beams. The signal and frequency are called beat signal and beat frequency, respectively. One of the most significant properties of HI is that the phase difference between the two beams, which is usually the most important quantity in interferometry, equals the phase of the beat signal. In conventional HI, the phase of the beat signal is measured by a single photodetector and a demodulation circuit or instrument. It is said that accuracy of phase measurement in HI reaches $2\pi/1000$ rad. Because of the nature of point-wise measurement, however, this method requires two-dimensional (2-D) scanning of the measured point to realize 2-D measurement, resulting in a trade-off between temporal and spatial resolution.

The objective of this article is to introduce a real-time 2-D HI technique. The key idea is the use of the time-domain correlation image sensor (CIS) (S. Ando, 2003) as a 2-D array of phase-demodulating pixels for incident heterodyne beams (A. Kimachi, 2007; 2010a). The CIS produces temporal correlations between the intensity signal of incident light and global reference signals over a frame period and outputs them as images at an ordinary frame rate. This property enables the CIS to simultaneously demodulate the amplitude and phase of the wavefront of incident heterodyne beams at each pixel in every frame using sinusoidal reference signals of the beat frequency. Consequently, as the most significant advantage, this real-time 2-D HI can ensure both maximal temporal and spatial resolution of the image sensor and high accuracy of phase measurement. Note that other than real-time 2-D HI, the CIS has opened a very wide range of novel applications such as image feature extraction (A. Kimachi, 1998), three-dimensional measurement (A. Kimachi, 2001; T. Kurihara, 2003; S. Ando, 2008a; A. Kimachi, 2009), optical flow measurement (S. Ando, 2008b), spectral matching imaging (A. Kimachi, 2002; 2004; 2010b), magneto-optic leakage flux imaging (S. Ando, 2007), and so forth.

The remainder of this article is organized as follows. Section 2 reviews previous studies on real-time 2-D HI and phase-shifting interferometry (PSI). Section 3 describes the principle of the CIS and the real-time 2-D HI. Section 4 shows experimental results of the real-time 2-D HI for a polarizing Michelson interferometer and speckle pattern interferometers for in-plane and out-of-plane deformation measurement. Section 5 briefly describes ongoing research on a

networked sensing system for health monitoring of large-scale structures based on multi-zero beams and the real-time 2-D HI. Finally, Section 6 concludes this article.

2. Review of real-time 2-D heterodyne and phase-shifting interferometry

A great number of studies have been devoted to the problem with HI mentioned in Section 1. Realization of real-time 2-D HI can be divided into two categories: 1) development of real-time PSI methods using image sensors, and 2) integration of phase-demodulating sensors into 2-D arrays. The following subsections briefly review studies belonging to each category.

2.1 Real-time PSI using image sensors

PSI, a widely-used interferometry technique realized with a commercial image sensor, is easier to deal with than the development of 2-D arrays of phase-demodulating sensors. PSI captures a sequence of fringe images formed by two interfering beams of the same frequency, while the phase difference between the beams is shifted stepwise with a piezoelectric actuator or a variable retarder in each frame (K.J. Gåsvik, 2002; J.H. Bruning, 1974). The original phase difference is estimated by fitting the intensity of the image sequence to a sine wave individually at each pixel (C.J. Morgan, 1982). PSI is used not only in ordinary interferometry for specularly reflective objects or transparent objects, but also in speckle pattern interferometry (SPI) (K. Creath, 1985; J. Kato, 1993; M. Takeda, 1994), optical coherence tomography (M. Akiba, 2003), or holography (I. Yamaguchi, 1997) for objects with rough surfaces or made of turbid media.

PSI requires three images at the minimum, and frequently employs four images with a phase shift increment by 90°. Higher accuracy is achieved for phase demodulation with a larger number of images; however, it results in a longer time for image capture. In PSI, temporal resolution and measurement accuracy are thus in a trade-off.

It seems that this problem with PSI could be solved by capturing fringe images with different phase shifts at the same time. North-Morris *et al.* (M. North-Morris, 2005) developed a phase mask consisting of an array of 2×2-pixel retarder matrices with $\pi/2$ steps of retardance for phase-shifting SPI. Four-step PSI is thus realized from a single-frame image by attaching this mask in front of an image sensor. A similar phase mask was proposed for phase-shifting holography by Awatsuji *et al.* (Y. Awatsuji, 2004). Kiire *et al.* (T. Kiire, 2008) proposed a method for simultaneously producing four separate images of speckle interference for different phase shifts on an image sensor using a polarizing prism, a diffraction grating, and two lasers of different wavelengths. The price for these single-frame PSI methods is, of course, loss of spatial resolution down to half of the image sensor.

Akiba *et al.* (M. Akiba, 2003) proposed a system of optical coherence tomography using two pairs of a liquid-crystal shutter and a CCD (charge coupled device) camera. The beat signal of low coherence interference exerted by a translating mirror is sampled in synchrony by the two shutters and integrated over a frame period of the CCDs at each pixel. This system captures a pair of phase-shifted fringe images at a video frame rate, though it may be categorized into 2-D discrete sampling of a continous beat signal as discussed in the next subsection rather than phase shifting. The phase of the beat signal can be obtained from the pair of integrated images and a dc component image captured beforehand, though phase demodulation was not performed in the paper. The accuracy of this method, however, can be degraded because of temporal sampling with a rectangular window, which has a certain degree of sensitivity to

higher-order harmonic components in the beat signal. Moreover, the two shutter-CCD pairs make the system rather bulky and demand cumbersome optical alignment.

2.2 Integration of 2-D phase-demodulating pixel arrays

Other studies focus on integrating real-time phase-demodulating pixels for HI into 2-D arrays. It is a straightforward idea to employ high-speed cameras as 2-D phase-demodulating arrays for sampling continuous beat signals at discrete time intervals (P. Haible, 2000; M.V. Aguanno, 2007). The higher the frame rate, the higher the accuracy of phase demodulation because of a larger number of samples, while the spatial resolution of the image sensor is maintained. The use of a high-speed camera, however, must be accompanied by a high-power laser source; otherwise it degrades the accuracy of phase demodulation because of shorter exposure time, lower light intensity, and hence lower signal-to-noise ratio (SNR) in the interference images. Moreover, high-speed cameras require high-speed frame grabber interface with large memory, which gives rise to a problem in terms of commercial availability.

Another group of studies employ 2-D arrays of phase-demodulating sensors developed on their own. A type of phase-demodulating image sensor called lock-in CCD, originally proposed by Spirig *et al.* (T. Spirig, 1995), outputs a set of discrete samples of the incident beat signal from each pixel, instead of a sequence of fringe images. The multiple samples are transferred to separate bins within a pixel as charge packets and accumulated over a frame period. The phase of the beat signal is demodulated from the set of samples at each pixel on a computer by the same algorithm as used in PSI. Dändliker *et al.* (R.D. Dändliker, 1998) used this sensor for distance interferometry. Earlier than these reports Povel *et al.* (H. Povel, 1990) devised a similar sensor for imaging polarimetry, though it was not named lock-in CCD.

It follows that in lock-in CCDs, the accuracy of phase demodulation, which increases for a larger number of samples or a higher sampling rate, is in a trade-off with spatial resolution because storing a large number of samples requires more space within the pixel on the sensor chip. Note also that the nature of discrete temporal sampling in lock-in CCDs as well as in high-speed cameras, represented by a rectangular temporal window function, again brings about the problem of sensitivity to higher-order harmonic components in the incident beat signal. This degradation becomes severer for a smaller number of samples or a lower sampling rate.

Another type of 2-D phase-demodulating pixel array was developed by Bourquin *et al.* for optical coherence tomography (S. Bourquin, 2001a). The pixel consists of a photodetector followed by a feedback circuit with a low-pass filter (LPF) and a rectifier (S. Bourquin, 2001b). For an incident beat signal of a frequency above the LPF cutoff frequency, the pixel can demodulate the signal amplitude as a result of open-loop operation of the feedback circuit. This sensor, however, cannot perform phase demodulation because it does not have the circuit for it.

Now the real-time 2-D HI presented in this article is compared to the techniques discussed so far. The CIS used in the real-time 2-D HI is exactly an ideal type of 2-D phase-demodulating pixel array. As a significant advantage over other techniques employing 2-D phase-demodulating pixel arrays and high-speed cameras, the CIS demodulates the phase of a continuous beat signal by continuous operation on analog circuitry under an ordinary frame rate, instead of discrete sampling and off-line computation. This property makes the real-time 2-D HI immune to the problems of rectangular windowing, light SNR, and frame

Type	Method/tool	Resolution		Accuracy	System issue
		Temporal	Spatial		
2-D heterodyne	Photodetector, 2-D scan	*	*	Good	
Phase shifting	Image sensor, phase shifter	*	Good	*	
Phase shifting	Two pairs of image sensor and electronic shutter	Good	Good	Fair	Alignment, bulkiness
Phase shifting	Image sensor with phase mask	Good	Poor	Fair	
Phase shifting	Phase-shifted images on one image sensor	Good	Poor	Fair	
2-D heterodyne (discrete)	High-speed camera	Good	Good	Fair	Light S/N, camera I/F
2-D heterodyne (discrete)	Lock-in CCD	Good	*	*	
2-D heterodyne	Correlation image sensor	Good	Good	Good	

Table 1. Comparison of 2-D HI and PSI techniques. The boxes with an asterisk in each row indicate a trade-off relation.

grabber interface. Moreover, spatial resolution can be maximally utilized as far as the pixel size permits, without any loss by sharing among multiple phase-shifted images, as is the case with the real-time PSI methods. The real-time 2-D HI and PSI techniques discussed above are summarized in Table 1.

3. Principle

This section first describes the principle of the CIS, and then explains how the CIS demodulates amplitude and phase images of heterodyne beams in real time.

3.1 Correlation image sensor

Figure 1(a) depicts the architecture of the CIS, which consists of a pixel array and three external inputs of reference signals supplied to all of the pixels. The pixel circuit for passive readout is illustrated in Figure 1(b) (S. Ando, 2003). The photodiode (PD) converts the incident light into a photocurrent $I(t)$ in proportion to its intensity $f_{ij}(t)$ at pixel (i,j). $I(t)$ is divided into three currents $I_k(t)$ ($k = 1,2,3$, $\sum_{k=1}^{3} I_k(t) = I(t)$) that flow through three NMOS transistors Q_k, and accumulated in three capacitors connected to the drains of Q_k over a frame period T. The balance among $I_k(t)$ depends on the gate voltages $V_k(t)$ as

$$I_k(t) = \rho g_k(t) I(t) + \frac{1}{3} I(t) \quad (k = 1,2,3), \tag{1}$$

where $g_k(t) = V_k(t) - \overline{V}$ denotes the differential component of $V_k(t)$ from the average $\overline{V} = \frac{1}{3}\sum_{k=1}^{3} V_k(t)$, and ρ is a constant. The signals $g_k(t)$, called reference signals, are supplied to the gates of Q_k in each pixel under a constraint $\sum_{k=1}^{3} g_k(t) = 0$. In Eq. (1), integrating $I_k(t)$

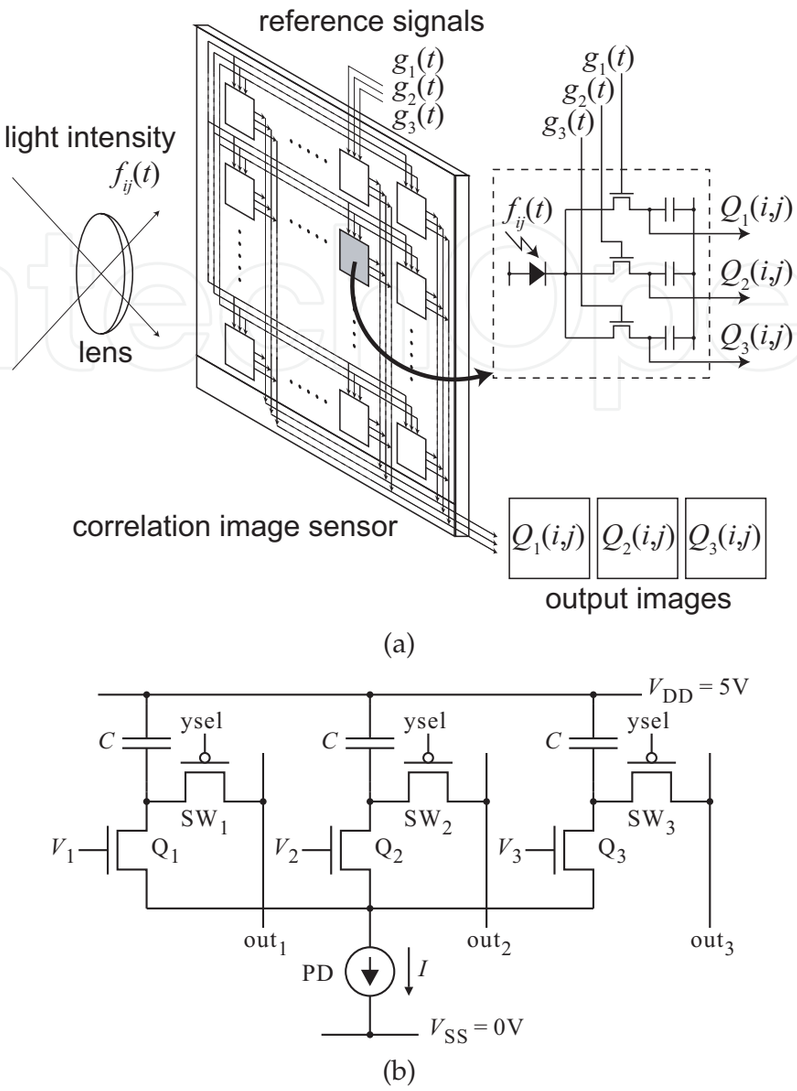

Fig. 1. Schematic of the CIS. (a) Overall architecture. (b) Pixel circuit for passive readout.

over T while redefining $\rho g_k(t)$ as $g_k(t)$ and replacing $I(t)$ with $f_{ij}(t)$ yields an expression for the accumulated charges $Q_k(i,j)$ as

$$\begin{aligned}\begin{bmatrix} Q_1(i,j) \\ Q_2(i,j) \\ Q_3(i,j) \end{bmatrix} &= \begin{bmatrix} \langle I_1(t) \rangle \\ \langle I_2(t) \rangle \\ \langle I_3(t) \rangle \end{bmatrix} \\ &= \begin{bmatrix} \Delta Q_1(i,j) \\ \Delta Q_2(i,j) \\ \Delta Q_3(i,j) \end{bmatrix} + \begin{bmatrix} \frac{1}{3}\langle f_{ij}(t) \rangle \\ \frac{1}{3}\langle f_{ij}(t) \rangle \\ \frac{1}{3}\langle f_{ij}(t) \rangle \end{bmatrix}, \end{aligned} \tag{2}$$

where $\langle \cdot \rangle$ denotes an integral over T. The term $\langle f_{ij}(t) \rangle$, obtained by

$$\langle f_{ij}(t) \rangle = \sum_{k=1}^{3} Q_k(i,j), \tag{3}$$

(a) (b)

Fig. 2. Photographs of CIS cameras with CMOS chips of (a) 64 × 64-pixel and (b) 200 × 200-pixel sensors.

is proportional to the average light intensity, as in conventional image sensors. The most significant difference from them is the term

$$\begin{aligned} \Delta Q_k(i,j) &= \langle f_{ij}(t) g_k(t) \rangle \\ &= Q_k(i,j) - \frac{1}{3}\langle f_{ij}(t) \rangle \quad (k = 1,2,3), \end{aligned} \tag{4}$$

which represents the temporal correlation between the intensity of the incident light $f_{ij}(t)$ and each of the reference signals $g_k(t)$. The three temporal correlations $\Delta Q_k(i,j)$ have two degrees of freedom under a constraint $\sum_{k=1}^{3} \Delta Q_k(i,j) = 0$ caused by $\sum_{k=1}^{3} g_k(t) = 0$. The charges $Q_k(i,j)$ are read out either passively through PMOS switches as shown in Figure 1(b) (S. Ando, 2003), or actively with voltage source followers (S. Han, 2010). Figure 2 shows photographs of CIS cameras with 64 × 64-pixel (S. Ando, 2003) and 200 × 200-pixel (S. Ando, 2007) CMOS chips of passive type.

3.2 Real-time amplitude and phase demodulation of heterodyne beams

Consider two heterodyne coherent beams with complex wavefronts u_{ij}, v_{ij} and a beat frequency $\Delta\nu$ to interfere on the focal plane of the CIS. The intensity $f_{ij}(t)$ of the interfering beams is given by

$$\begin{aligned} f_{ij}(t) &= |u_{ij} + v_{ij} \exp[\mathrm{i}2\pi\Delta\nu t]|^2 + n_{ij}(t) \\ &= A_{ij} \cos(\omega t + \theta_{ij}) + B_{ij} + n_{ij}(t), \\ A_{ij} &= 2|u_{ij}||v_{ij}|, \quad \theta_{ij} = \angle v_{ij} - \angle u_{ij}, \quad B_{ij} = |u_{ij}|^2 + |v_{ij}|^2, \quad \omega = 2\pi\Delta\nu, \end{aligned} \tag{5}$$

where i denotes the imaginary unit ($\mathrm{i}^2 = -1$) and background illumination $n_{ij}(t)$ is taken into account. The beat frequency $\Delta\nu$ is chosen to be a multiple of the frame rate of the CIS, $\Delta\nu = mT^{-1}$ (m: integer), or much higher than the frame rate, $\Delta\nu \gg T^{-1}$. The interference amplitude A_{ij} and phase θ_{ij} are simultaneously demodulated from single-frame temporal correlation images $\Delta Q_k(i,j)$, by supplying the CIS with three-phase reference signals $g_k(t)$ of the same

angular frequency ω expressed by

$$\begin{bmatrix} g_1(t) \\ g_2(t) \\ g_3(t) \end{bmatrix} = \begin{bmatrix} \cos \omega t \\ \cos\left(\omega t + \frac{2}{3}\pi\right) \\ \cos\left(\omega t + \frac{4}{3}\pi\right) \end{bmatrix}. \tag{6}$$

Noting that the average intensity B_{ij} and the background illumination $n_{ij}(t)$ are both uncorrelated with the sinusoudal reference signals $g_k(t)$, i.e. $\langle g_k(t)B_{ij}\rangle = \langle g_k(t)n_{ij}(t)\rangle = 0$, substitution of Eqs. (5) and (6) into Eq. (4) under the condition $\Delta\nu = mT^{-1}$ or $\Delta\nu \gg T^{-1}$ yields the single-frame temporal correlation images $\Delta Q_k(i,j)$ as

$$\begin{bmatrix} \Delta Q_1(i,j) \\ \Delta Q_2(i,j) \\ \Delta Q_3(i,j) \end{bmatrix} = \frac{TA_{ij}}{2} \begin{bmatrix} \cos\theta_{ij} \\ \cos\left(\theta_{ij} - \frac{2}{3}\pi\right) \\ \cos\left(\theta_{ij} - \frac{4}{3}\pi\right) \end{bmatrix} + \begin{bmatrix} \xi_1(i,j) \\ \xi_2(i,j) \\ \xi_3(i,j) \end{bmatrix}, \tag{7}$$

where noise contributions $\xi_k(i,j)$ are taken into account. The interference amplitude A_{ij} and phase θ_{ij} are obtained from $\Delta Q_k(i,j)$ by least-squares estimation as

$$\theta_{ij} = \tan^{-1}\frac{\sqrt{3}(\Delta Q_2 - \Delta Q_3)}{2\Delta Q_1 - \Delta Q_2 - \Delta Q_3}, \tag{8}$$

$$A_{ij} = \frac{2\sqrt{2}}{3T}[(\Delta Q_1 - \Delta Q_2)^2 + (\Delta Q_2 - \Delta Q_3)^2 + (\Delta Q_3 - \Delta Q_1)^2]^{1/2}, \tag{9}$$

where (i,j) is dropped for notational symplicity.

4. Experimental results

The theory on real-time 2-D HI using the CIS described in Section 3 are verified on two types of interferometer—a Michelson interferometer and speckle pattern interferometers for in-plane and out-of-plane deformation measurement.

4.1 Real-time heterodyne Michelson interferometry

To study the feasibility of the proposed real-time 2-D HI, a heterodyne polarizing Michelson interferometer was constructed with the CIS as depicted in Figure 3(a) (A. Kimachi, 2007). A pair of orthogonally-polarized heterodyne beams coaxially enter the interferometer through a beam expander L1. The beams are split by the polarizing beam splitter PBS1 and reflected on the mirrors M1 and M2 while passing through the quarter wave plates QWP1 and QWP2 twice, which rotate the polarization of each reflected beam by 90°. The reflected beams are merged by PBS1 and interfere on the CIS through an analyzer POL1 and an imaging lens L2. A reference beat signal is generated by taking out a small portion of the heterodyne beams with a beam splitter BS and detecting the interference intensity with a photodiode PD. This signal is converted into three-phase sinusoidal reference signals for the CIS. The heterodyne beams are emitted from a commercial two-frequency He-Ne laser source shown in Figure 3(b) (wavelength $\lambda = 632.8$ nm), which consists of two acousto-optic modulators driven at slightly different frequencies to yield a beat frequency of $\Delta\nu = 25$ kHz. The mirror M1 is longitudinally moved with a piezoelectric actuator under open-loop control to change the interference phase θ_{ij} between the two beams linearly to the displacement δz.

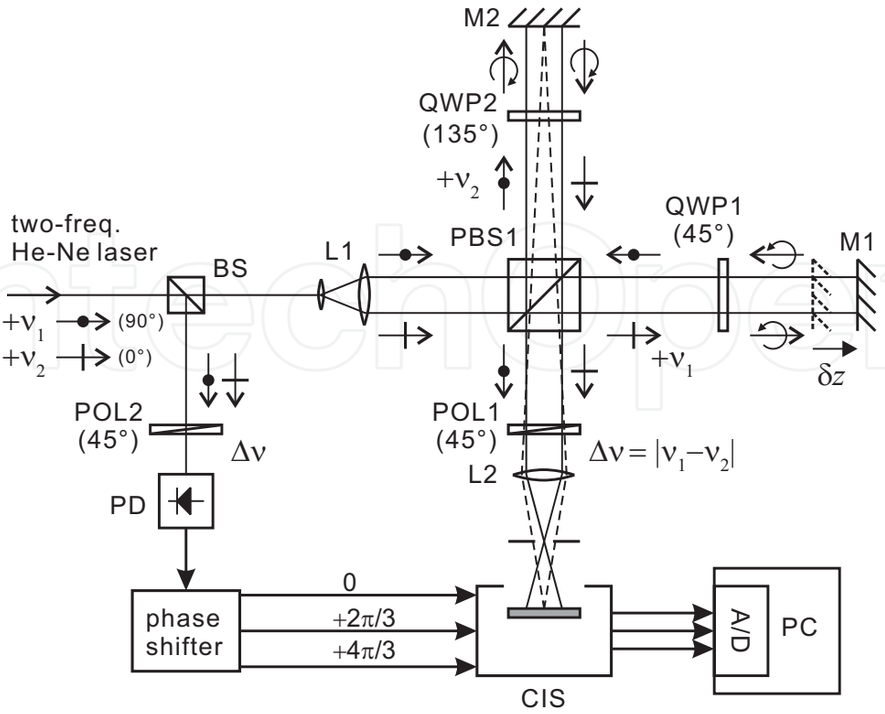

(a)

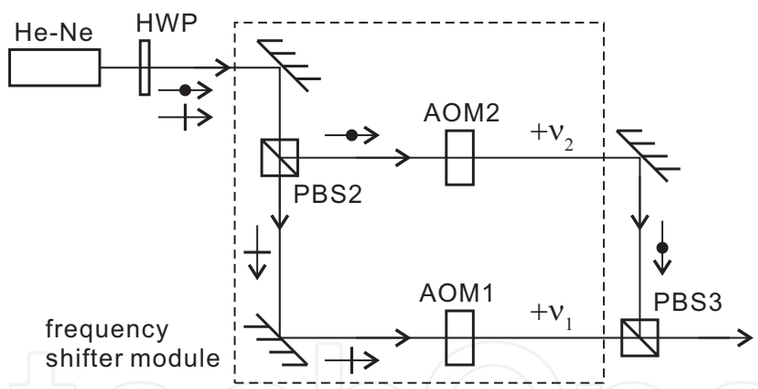

(b)

Fig. 3. Schematic of the real-time heterodyne polarizing Michelson interferometer with the CIS (A. Kimachi, 2007). (a) Interferometer optics. BS: beam splitter; PBS: polarizing beam splitter; QWP: quarter-wave plate; POL: polarizer/analyzer; PD: photodiode. (b) Two-frequency He-Ne laser source. AOM: acousto-optic modulator; HWP: half-wave plate.

The 64×64-pixel CIS in Figure 2(a) was used in the interferometer in Figure 3(a), operating at a frame rate of $T^{-1} = 30$ fps ($\ll \Delta\nu$). Figure 4 shows an example of average intensity, demodulated amplitude, and demodulated phase images computed from the raw output images $Q_k(i,j)$ with Eqs. (3), (4), (8) and (9) (A. Kimachi, 2007). The demodulated phase θ_{ij} in Figure 4(c) is coded in gray scale as depicted in Figure 4(d). The abrupt edge from black to white in Figure 4(c) corresponds to a 2π jump.

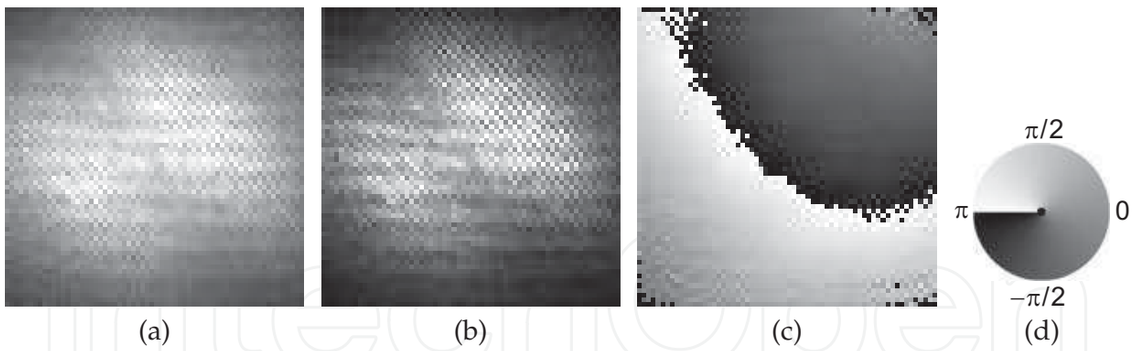

Fig. 4. An example of output images from the 64 × 64-pixel CIS in the real-time heterodyne Michelson interfereometer (A. Kimachi, 2007). (a) Average intensity $\langle f_{ij}(t)\rangle$. (b) Demodulated amplitude A_{ij}. (c) Demodulated phase θ_{ij}. (d) Gray-scale representation of phase.

Figure 5 shows the results when the mirror M1 was moved by the deformation of the piezoelectric actuator for changes in voltage (A. Kimachi, 2007). Figure 5(a) shows a sequence of demodulated phase images for voltages from 30.0 V to 36.5 V in 0.5-V steps. The difference of each phase image from that for 30.0 V is shown in Figure 5(b). The phase difference for the pixel at the image center is unwrapped and plotted in Figure 5(c) up to 50.0 V, along with a linear fit. The plot in Figure 5(c) exhibits a good linear response to the applied voltage, which is ideally linear to the displacement of M1, despite the open-loop control of the piezoelectric actuator. The slope of the linear fit in Figure 5(c) amounts to 65 nm/V in terms of optical path length, which is close to the characteristic of the piezoelectric actuator (61 nm/V).

The real-time heterodyne Michelson interfereometer in Figure 3 was applied to monitoring dynamic change in the interference phase of the heterodyne beams, which was caused by silicone oil inserted in front of the mirror M1 as depicted in Figures 6(a) and (b). Figure 6(c) shows a real-time sequence of phase difference images in every 0.2 s, i.e. every six frames, with respect to the initial state, while the silicone oil was heated by the heating cable (A. Kimachi, 2007). It is observed that gradation is buidling up near the surface of the silicone oil as time passes, suggesting changes in refractive index due to increase in temperature as well as convection that brings heated silicone oil up toward the surface.

4.2 Real-time heterodyne speckle pattern interferometry

The real-time 2-D HI was also applied to SPI. Figure 7(a) depicts a real-time heterodyne SPI system for in-plane deformation measurement (A. Kimachi, 2010a). The heterodyne beams are generated by a He-Ne laser and an electro-optic modulator (EOM), which shifts the phase between a pair of orthogonally-polarized coaxial beams from 0 to 2π linearly to time at a frequency of $\Delta\nu = 100$ Hz by a sawtooth-shaped driving voltage signal. The heterodyne beams are split by the polarizing beam splitter PBS and projected onto the object from symmetrically opposite directions with an inclination angle $\alpha = 45^\circ$. The interference speckle pattern generated on the object is imaged through an analyzer POL onto the CIS, which is supplied with three-phase reference signals of the same frequency $\Delta\nu$ as that of the EOM driving signal. The CIS demodulates the phase of the interference speckle pattern from single-frame output images, yielding a random pattern. The difference of the demodulated phase from that of the object at an initial state changes linearly to the in-plane deformation δx

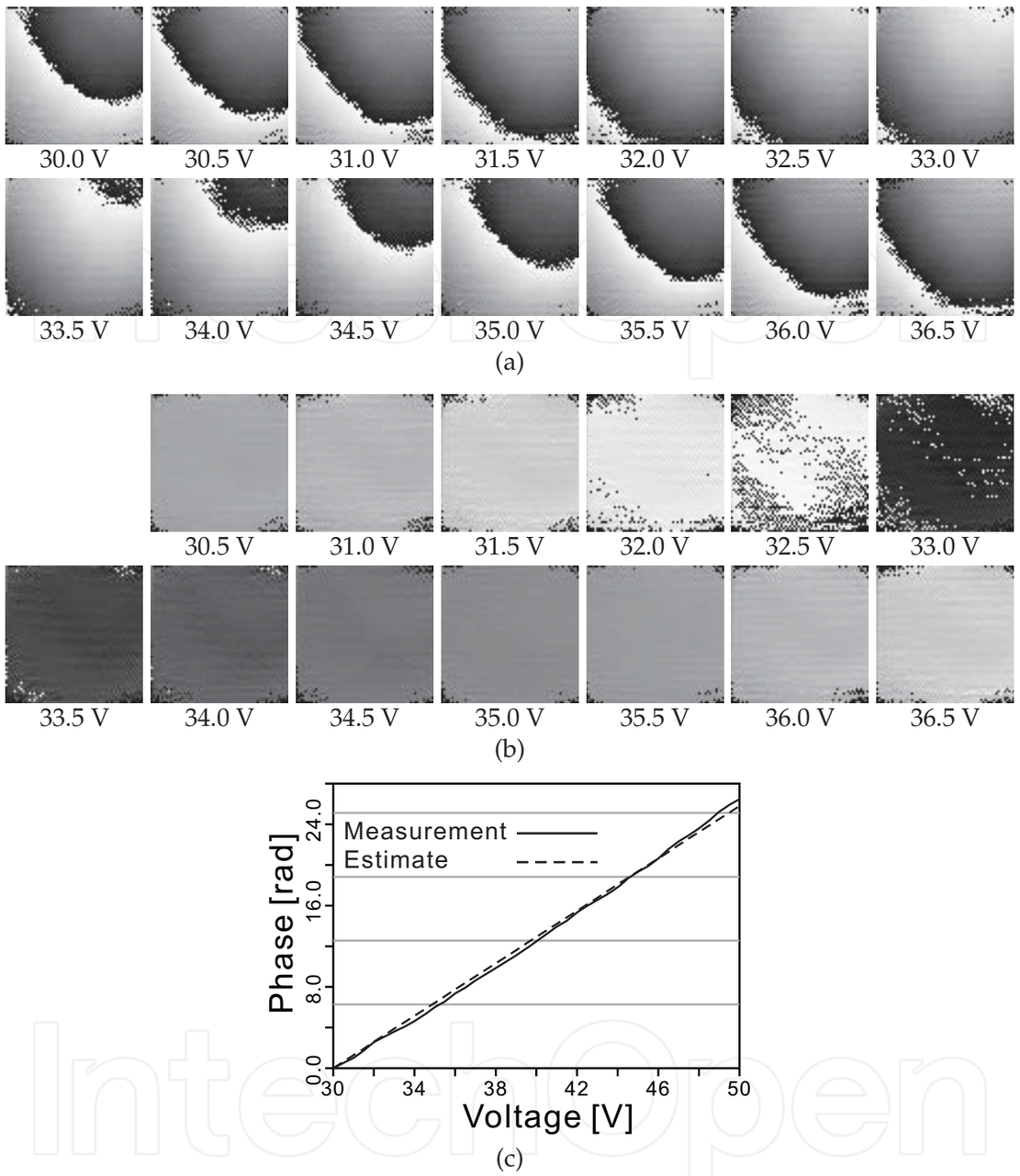

Fig. 5. Results of the real-time heterodyne Michelson interferometer for changes in the piezoelectric actuator's voltage (A. Kimachi, 2007). (a) Demodulated phase images. (b) Images of phase difference with respect to 30.0 V. (c) Plot of the unwrapped phase difference at a pixel at the image center.

at each pixel, as long as the deformation does not exceed the average speckle size to escape speckle decorrelation.

The 200 $\times$ 200-pixel CIS camera in Figure 2(b) was used in the SPI system in Figure 7(a), operating at a frame rate of $T^{-1} = 8.33$ fps ($= \Delta\nu/12$). Figure 8 shows the results for a

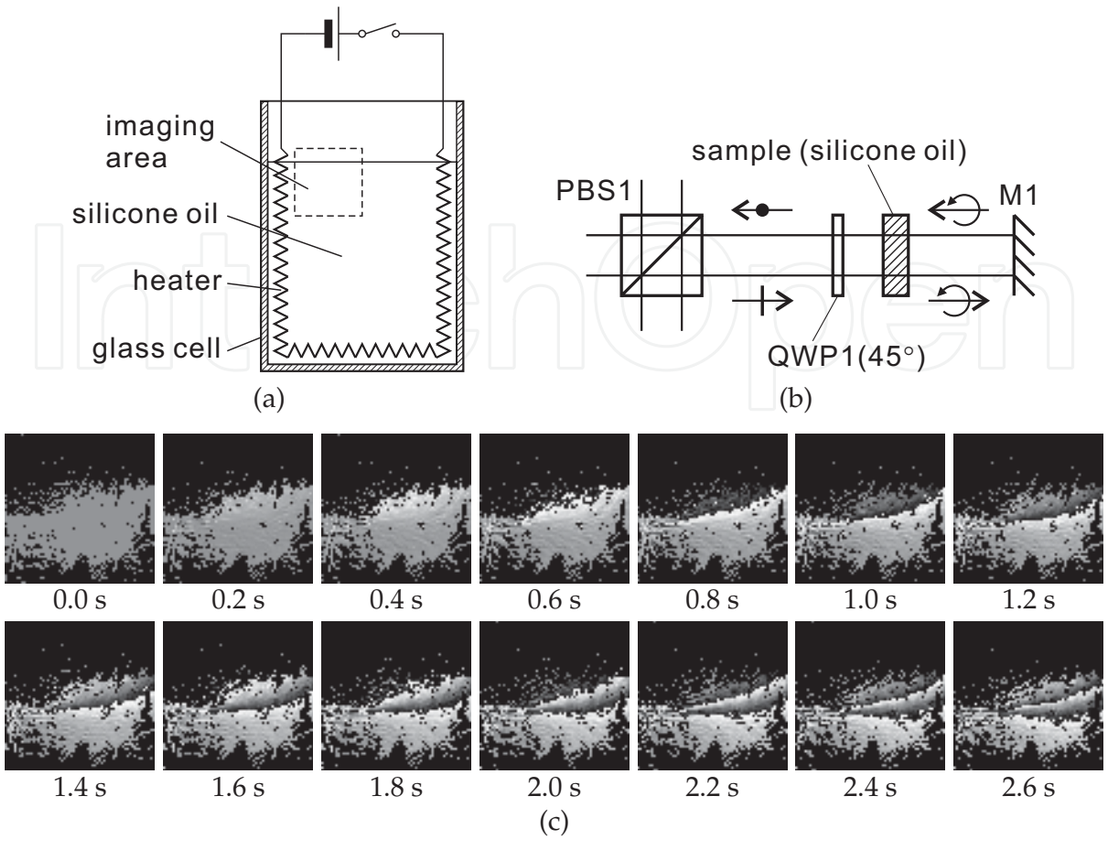

Fig. 6. Results on the real-time heterodyne Michelson interferometer for an object under dynamic behavior (A. Kimachi, 2007). (a) Illustration of the object. (b) Optical arrangement of the object. (c) Real-time sequence of phase difference images with respect to 0.0 s while the object was heated.

flat object with a rough surface while it was moved in an in-plane direction in 40-nm steps by a nano-scale linear stage (A. Kimachi, 2010a). Figure 8(a) shows a sequence of phase difference images with respect to the initial position of the object, smoothed with a 5×5-pixel Gaussian filter. The value of phase difference is coded again as in Figure 4(d). The images exhibit gradual changes in phase difference in accordance with the in-plane displacement. The average and standard deviation of unwrapped phase difference over the central 50×50-pixel region are plotted in Figure 8(b) along with a theoretical response, up to the displacement of 2 μm. The plot of the average phase difference agrees well with the theoretical response. The standard deviation was 0.13 rad, or 9 nm in terms of displacement, in average over the plotted range.

A similar experiment was carried out as well for the real-time heterodyne SPI system for out-of-plane deformation measurement depicted in Figure 7(b), which is based on a Michelson interferometer with the reflection mirrors replaced by the object and a reference plate with a rough surface (A. Kimachi, 2010a). The same 200×200-pixel CIS camera, heterodyne laser source, and flat object were used as in the system in Figure 7(a). Figure 9(a) shows a sequence of phase difference images with respect to the initial position of the object, while it underwent out-of-plane displacement along the optical axis in 40-nm steps. The images exhibit gradual

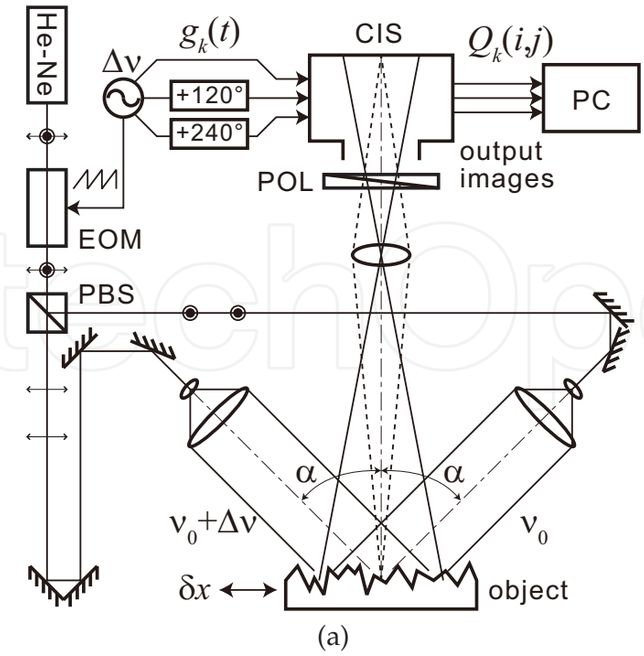

(a)

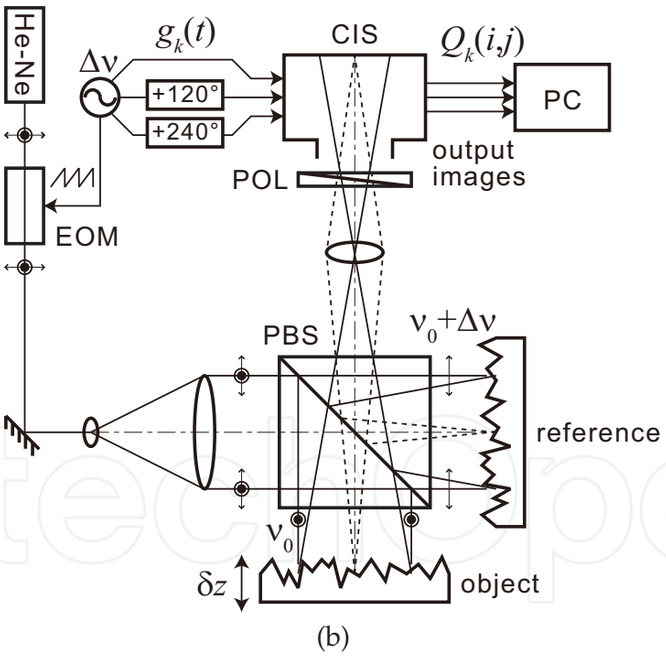

(b)

Fig. 7. Schematics of the real-time heterodyne SPI systems with the CIS for (a) in-plane, and (b) out-of-plane deformation measurement (A. Kimachi, 2010a).

changes in phase difference, as observed in Figure 8(a), though they look a little noisier. The average and standard deviation of unwrapped phase difference over the central 50 × 50-pixel region are plotted in Figure 9(b), along with a theoretical response. The standard deviation was 0.33 rad, or 17 nm in terms of displacement, in average over the plotted range, which is larger than the plot in Figure 8(b). Moreover, the agreement between the experimental and

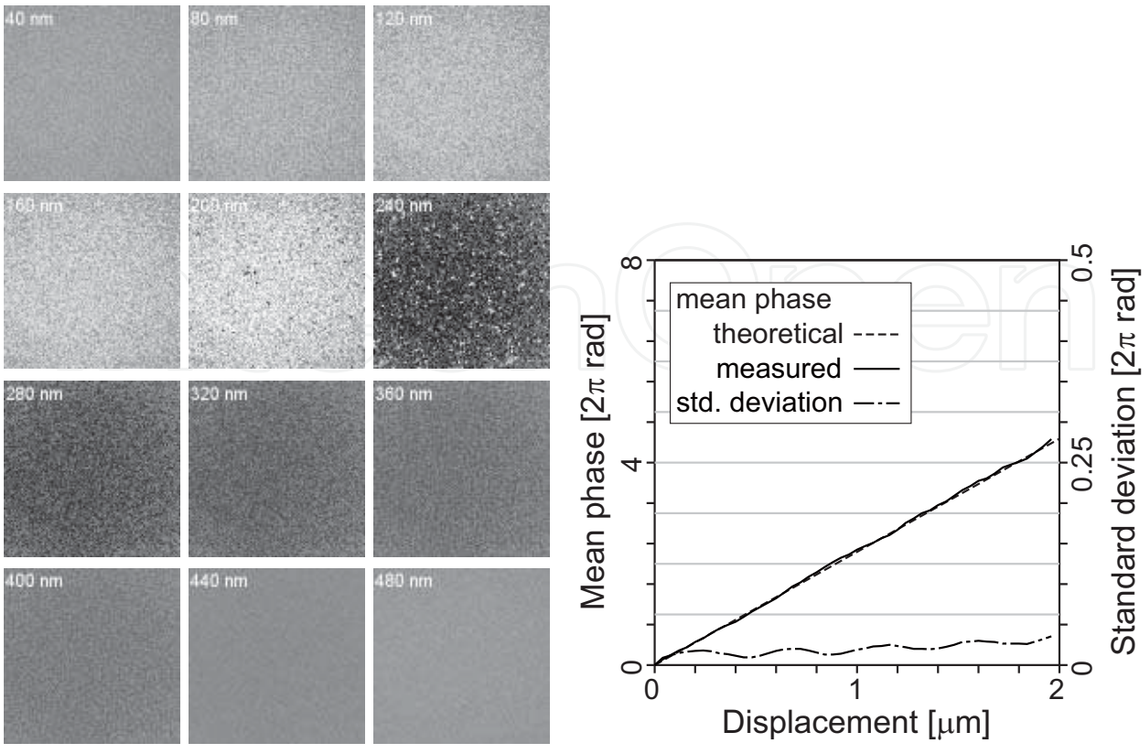

(a) (b)

Fig. 8. Results of the real-time heterodyne SPI system for in-plane displacement of a flat object with a rough surface (A. Kimachi, 2010a). (a) Sequence of phase difference images with respect to the initial position of the object, for displacement increasing in 40-nm steps. (b) Average and standard deviation of the images of unwrapped phase difference within a central 50×50-pixel region, along with a theoretical response.

theoretical plots is not as good as that for the in-plane displacement in Figure 8(b), exhibiting a drift of the experimental plot from the theoretical one. These observations can be attributed to the nature of the Michelson interferometer the SPI system in Figure 7(b) is based on, which involves two separate reflective objects and is thus more sensitive to disturbance than the SPI system for in-plane deformation in Figure 7(a).

The real-time heterodyne SPI system for in-plane deformation in Figure 7(a) was employed for monitoring an object under dynamic deformation. The object is a piezoelectric actuator placed horizontally and attached to a fixed frame, as depicted in Figure 10(a). Figure 10(b) shows a real-time sequence of phase difference images in every 0.12-s frame with respect to the initial state, featuring the junction between the object and fixed frame. The profile of the images along the horizontal white line is plotted in Figure 10(c). The left-hand side of the plot, corresponding to the actuator, exhibits a continuous increase in the slope as well as a gradual upward shift. The increasing slope indicates that the actuator is expanding toward the left, whereas the upward shift implies that the actuator itself also slides to the left. The right-hand side of the plot, corresponding to the fixed frame, exhibits a gradual downward shift of much smaller steps than that for the actuator. This suggests the existence of a strong force by the actuator that slightly pushes the fixed frame in the opposite direction to its expanding direction.

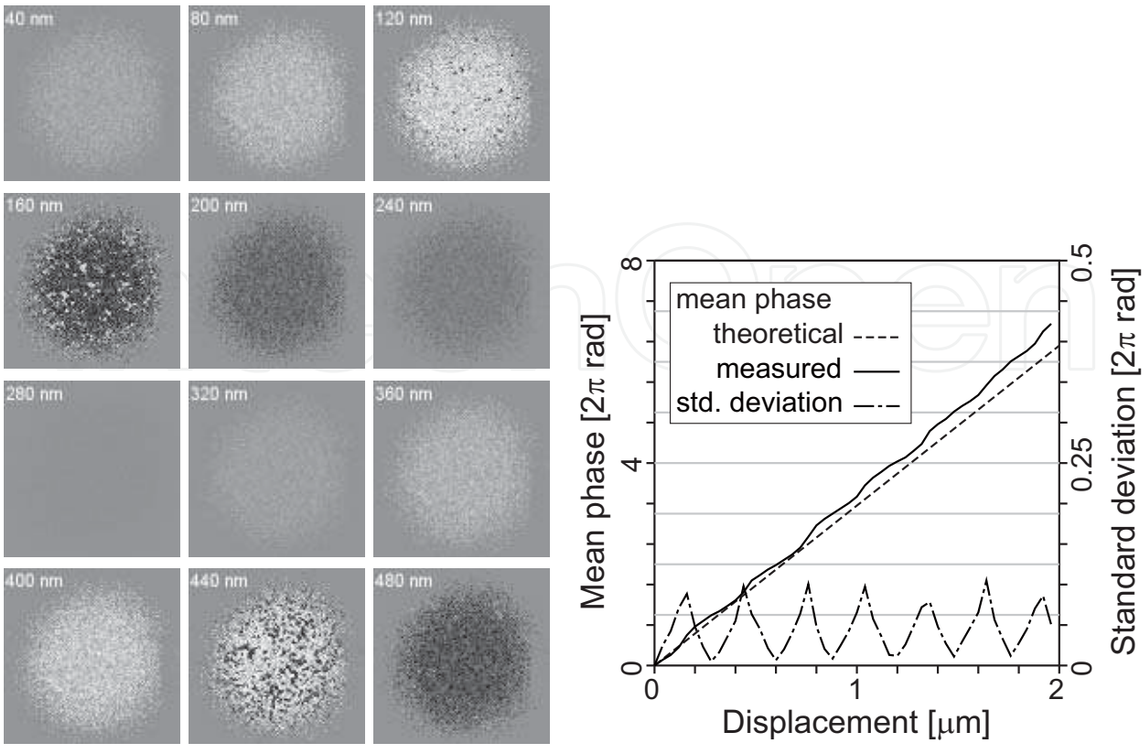

(a) (b)

Fig. 9. Results on the real-time heterodyne SPI system for out-of-plane displacement of a flat object with a rough surface (A. Kimachi, 2010a). (a) Sequence of phase difference images with respect to the initial position of the object, for displacement increasing in 40-nm steps. (b) Average and standard deviation of the images of unwrapped phase difference within a central 50×50-pixel region, along with a theoretical response.

5. Application to a health monitoring system for large-scale structures

The real-time 2-D HI described in the previous sections is particularly effective in applications that require not only high accuracy but also real-time 2-D phase measurement. As one of such applications, a research project on health monitoring of large-scale structures has been promoted by Ando *et al.* (S. Sato, 2008a;b;c; S. Ando, 2009). This project aims at developing a networked sensing system that can measure relative deformation of large-scale structures such as bridges, tunnels, industrial plants and tall buildings in real time and at high accuracy over three axes of displacement and three axes of rotation. This kind of sensing system is drawing increasing attention because large-scale structures can cause catastrophic disasters when they are broken down from aging, fatigue, or defects. Health monitoring of large-scale structures, however, is not easy because they are located outdoors in tough enviroment and their size makes it very laborious to inspect the whole entity for defects.

As a solution to this problem, a networked sensing system that employs the real-time 2-D HI has been proposed (S. Sato, 2008a;b;c). The sensor network is comprised of a train of sensing units placed over a large-scale structure. The sensing unit consists of a pair of a CIS chip and a heterodyne laser source, and transmits coaxial heterodyne laser beams to one neighboring unit while receiving coaxial heterodyne laser beams from another neighboring unit. The

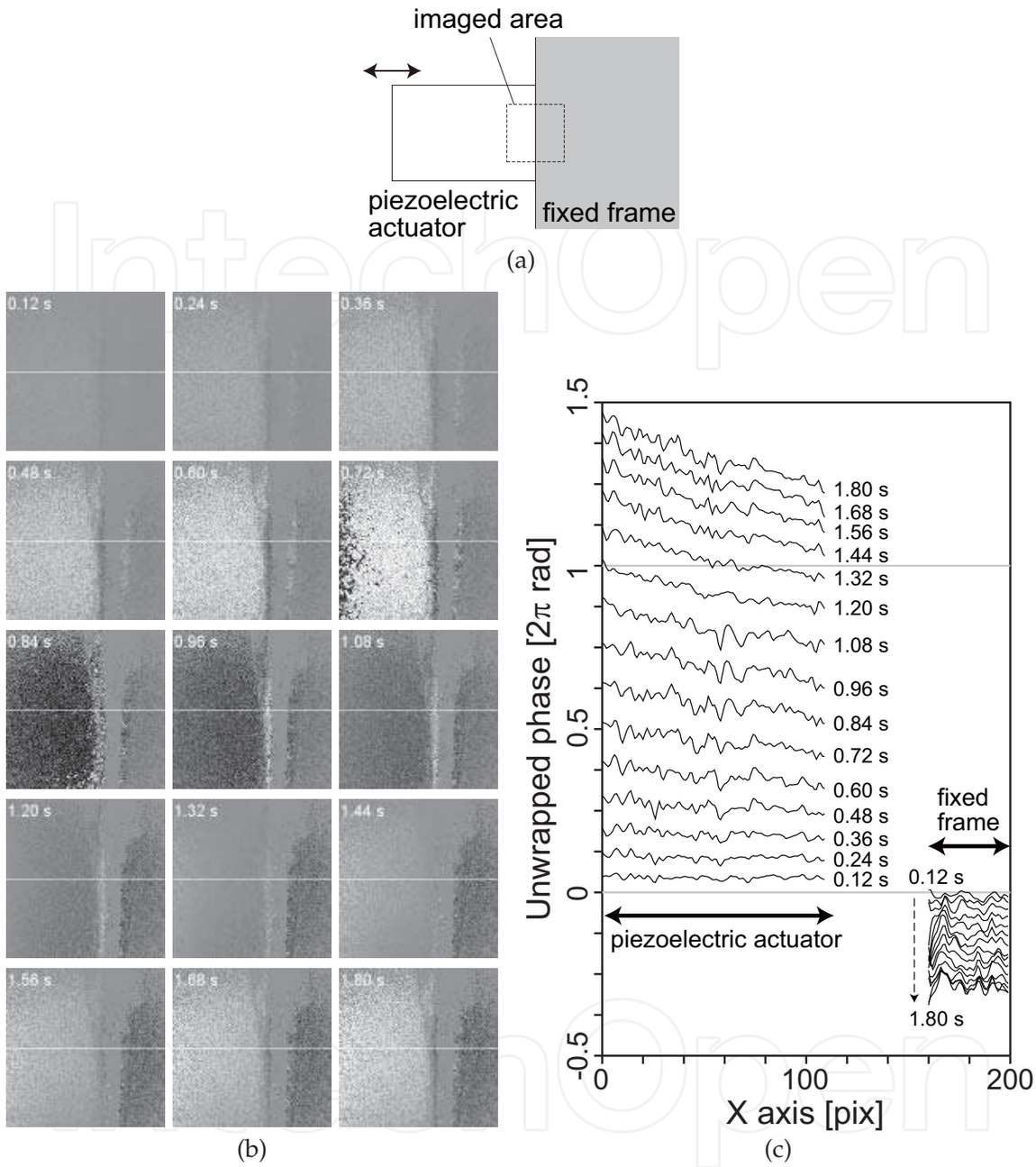

Fig. 10. Results of real-time heterodyne SPI for an object under dynamic in-plane deformation (A. Kimachi, 2010a). (a) Illustration of the object. (b) Real-time sequence of phase difference images with respect to 0.0 s while the object was horizontally expanded. (c) Profiles of unwrapped phase difference along the horizontal white lines in the images.

entire deformation of a large-scale structure can be obtained by integrating the relative six-axis deformation between each transmitter-receiver pair of sensing units over the network.

The key idea for measuring the relative deformation between a pair of sensing units lies in the use of multi-zero beams (S. Sato, 2008a;b;c), which have a wavefront with multiple

zeros distributed over the beam area. The relative deformation can be known from a change in the amplitude and phase pattern of a multi-zero wavefront, which is easily detected on the CIS chip by the real-time 2-D HI at high accuracy. The multi-zero beams, which are generated by multiplexing Laguerre-Gaussian (LG) beams of different orders, have been found from extensive studies to possess many characteristics suitable for measurement and sensing (S. Sato, 2008a;b;c).

Based on these ideas, several experimental systems have been so far developed and tested in experiments on real-time tracking of multi-zeros (S. Ando, 2009). This project is currently at the stage of the development of a prototype system and the experimental evaluation on actual large-scale structures.

6. Conclusion

The real-time 2-D HI technique presented in this article is based on the use of the CIS as a two-dimensional array of pixels, each of which simultaneously demodulate the amplitude and phase of incident heterodyne beams at an ordinary frame rate. As the most significant advantage over other real-time 2-D HI or PSI techniques, the CIS-based technique ensures both maximal temporal and spatial resolution and high accuracy of phase measurement. The experimental results obtained on a polarizing Michelson interferometer and speckle pattern interferometers for in-plane and out-of-plane deformation measurement confirm the feasibility and usefulness of the real-time 2-D HI. The real-time 2-D HI is expected to find many application areas such as the health monitoring system for large-scale structures based on multi-zero beams.

7. References

R. Dändliker, B. Ineichen and F.M. Mottier, "High-Resolution Hologram Interferometry by Electronic Phase Measurement," *Opt. Commun.*, vol. 9, pp. 412-416, 1973.

N.A. Massie, R.D. Nelson and S. Holly, "High-Performance Real-Time Heterodyne Interferometry," *Appl. Opt.*, vol. 18, pp. 1797-1803, 1979.

S. Ando and A. Kimachi, "Correlation Image Sensor: Two-Dimensional Matched Detection of Amplitude-Modulated Light," *IEEE Trans. Electron Devices*, vol. 50, pp. 2059-2066, 2003.

A. Kimachi, "Real-Time Heterodyne Imaging Interferometry: Focal-Plane Amplitude and Phase Demodulation Using a Three-Phase Correlation Image Sensor," *Appl. Opt.*, vol. 46, pp. 87-94, 2007.

A. Kimachi, "Real-Time Heterodyne Speckle Pattern Interferometry Using the Correlation Image Sensor," *Appl. Opt.*, vol. 49, pp. 6808-6815, 2010.

A. Kimachi, R. Imaizumi and S. Ando, "Intelligent Image Sensor with a Vibratory Mirror Mimicking Involuntary Eye Movement," in *Tech. Digest of 16th Sensor Symp.*, pp. 171-176, Kawasaki, Japan, 1998.

A. Kimachi, T. Kurihara, M. Takamoto and S. Ando, "A Novel Range Finding System Using Correlation Image Sensor," *Trans. IEE Japan*, vol. 121-E, pp. 367-375, 2001.

T. Kurihara, N. Ono and S. Ando, "Surface Orientation Imager Using Three-Phase Amplitude-Modulated Illumination and Correlation Image Sensor," in *Proc. SPIE*, vol. 5013, pp. 95-102, 2003.

S. Ando and N. Ono, "Spatio-Temporal Phase-Encoding Profilometry Using Correlation Image Sensor," in *Proc. IEEE Int. Symp. Industrial Electronics*, pp. 786-791, Cambridge, U.K., 2008.

A. Kimachi and S. Ando, "Real-Time Phase-Stamp Range Finder Using Correlation Image Sensor," *IEEE Sensors J.*, vol. 9, pp. 1784-1792, 2009.

S. Ando, T. Kurihara and D. Wei, "Optical Flow Sensor with Maximal Spatio-Temporal Resolution," in *Proc. 25th Sensor Symp.*, pp. 683-688, Ginowan, Japan, 2008.

A. Kimachi, T. Imaizumi, A. Kato and S. Ando, "Spectral Matching Imager Using Correlation Image Sensor," *Trans. IEE Japan*, vol. 122-E, pp. 200-206, 2002.

A. Kimachi, H. Ikuta, Y. Fujiwara, M. Masumoto and H. Matsuyama, "Spectral Matching Imager Using Amplitude-Modulation-Coded Multispectral Light-Emitting Diode Illumination," *Opt. Eng.*, vol. 43, pp. 975-985, 2004.

A. Kimachi, S. Ando, M. Doi and S. Nishi, "Spectral Matching Imager with Three-Phase Quadrature Detection," in *Proc. SPIE*, vol. 7528, pp. 75280E-1-9, 2010.

S. Ando, T. Nara, N. Ono and T. Kurihara, "Real-Time Orientation-Sensitive Magnetooptic Imager for Leakage Flux Inspection," *IEEE Trans. Magnetics*, vol. 43, pp. 1044-1051, 2007.

K.J. Gåsvik, *Optical Metrology*, 3rd ed. Wiley: Chichester, 2002.

J.H. Bruning, D.R. Herriott, J.E. Gallagher, D.P. Rosenfeld, A.D. White and D.J. Brangaccio, "Digital Wavefront Measuring Interferometer for Testing Optical Surfaces and Lenses," *Appl. Opt.*, vol. 13, pp. 2693-2703, 1974.

C.J. Morgan, "Least-Squares Estimation in Phase-Measurement Interferometry," *Opt. Lett.*, vol. 7, pp. 368-370, 1982.

K. Creath, "Phase-Shifting Speckle Interferometry," *Appl. Opt*, vol. 24, pp. 3053-3058, 1985.

J. Kato, I. Yamaguchi and Q. Ping, "Automatic Deformation Analysis by a TV Speckle Interferometer Using a Laser Diode," *Appl. Opt*, vol. 32, pp. 77-83, 1993.

M. Takeda and H. Yamamoto, "Fourier-Transform Speckle Profilometry: Three-Dimensional Shape Measurements of Diffuse Objects with Large Height Steps and/or Spatially Isolated Surfaces," *Appl. Opt.*, vol. 33, pp. 7829-7837, 1994.

M. Akiba, K.P. Chan, and N. Tanno, "Full-Field Optical Coherence Tomography by Two-Dimensional Heterodyne Detection with a Pair of CCD Cameras," *Opt. Lett.*, vol. 28, pp. 816-818, 2003.

I. Yamaguchi and T. Zhang, "Phase-Shifting Digital Holography," *Opt. Lett.*, vol. 22, pp. 1268-1270, 1997.

M. North-Morris, J. Millerd, N. Brock, J. Hayes and B. Saif, "Dynamic Phase-Shifting Electronic Speckle Pattern Interferometer," in *Proc. SPIE*, vol. 5869, 58691B, 2005.

Y. Awatsuji, M. Sasada and T. Kubota, "Parallel Quasi-Phase-Shifting Digital Holography," *Appl. Phys. Lett.*, vol. 85, pp. 1069-1071, 2004.

T. Kiire, S. Nakadate and M. Shibuya, "Simultaneous Formation of Four Fringes by Using a Polarization Quadrature Phase-Shifting Interferometer with Wave Plates and a Diffracetion Grating," *Appl. Opt.*, vol. 47, pp. 4787-4792, 2008.

P. Haible, M.P. Kothiyal and H.J. Tiziani, "Heterodyne Temporal Speckle-Pattern Interferometry," *Appl. Opt.*, vol. 39, pp. 114-117, 2000.

M.V. Aguanno, F. Lakestani, M.P. Whelan and M.J. Connelly, "Heterodyne Speckle Interferometer for Full-Field Velocity Profile Measurements of a Vibrating Menbrane by Electronic Scanning," *Opt. Lasers Eng.*, vol. 45, pp. 677-683, 2007.

T. Spirig, P. Seitz, O. Vietze and F. Heitger, "The Lock-in CCD—Two-Dimensional Synchronous Detection of Light," *IEEE J. Quantum Electronics*, vol. 31, pp. 1705-1708, 1995.

R. Dändliker, Y. Salvadé and E. Zimmermann, "Distance-Measurement by Multiple-Wavelength Interferometry," *J. Opt.*, vol. 29, pp. 105-114, 1998.

H. Povel, H. Aebersold and J.O. Stenflo, "Charge-Coupled Device Image Sensor as a Demodulator in a 2-D Polarimeter with a Piezoelastic Modulator," *Appl. Opt.*, vol. 29, pp. 1186-1190, 1990.

S. Bourquin, P. Seitz, and R.P. Salathé, "Optical Coherence Topography Based on a Two-Dimensional Smart Detector Array," *Opt. Lett.*, vol. 26, pp. 512-514, 2001.

S. Bourquin, P. Seitz, and R.P. Salathé, "Two-Dimensional Smart Detector Array for Interferometric Applications," *Electron. Lett.*, vol. 37, pp. 975-976, 2001.

S. Han, T. Sawada, T. Iwahori, S. Kawahito and S. Ando, "Three-Phase Time-Correlation Image Sensor Using Pinned Photodiode Active Pixels," in *Proc. SPIE*, vol. 7536, 2010.

S. Sato, I. Fujimoto, T. Kurihara and S. Ando, "Remote Six-Axis Deformation Sensing with Optical Vortex Beams," in *Proc. SPIE*, vol. 6877, 2008.

S. Sato, I. Fujimoto, T. Kurihara and S. Ando, "Optical Vortex and Correlation Image Sensor for Networked Deformation Sensing of Infrastructures," in *Proc. 5th Int. Conf. Networked Sensing Systems*, pp. 39-42, Kanazawa, Japan, 2008.

S. Sato, I. Fujimoto, T. Kurihara and S. Ando, "Remote Full-Axis Deformation Sensing with Optical Vortex Beam for Health Monitoring of Infrastructures," in *Proc. 3rd Int. Conf. Sensing Technology*, pp. 452-456, Tainan, Taiwan, 2008.

S. Ando, S. Sato and T. Kurihara, "Real-Time Tracking Experiment of Higher-Order Laguerre-Gaussian Beam for Remote Six-Axis Deformation Sensing," in *Proc. Sixth Int. Conf. Networked Sensing Systems*, pp. 1-4, Pittsburgh, PA, 2009.

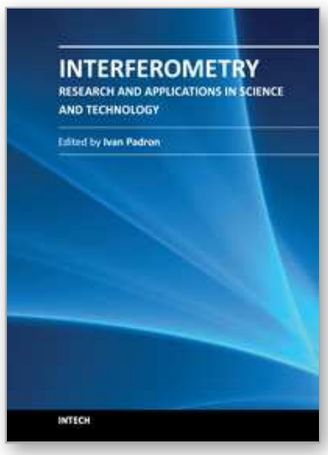

Interferometry - Research and Applications in Science and Technology

Edited by Dr Ivan Padron

ISBN 978-953-51-0403-2
Hard cover, 462 pages
Publisher InTech
Published online 21, March, 2012
Published in print edition March, 2012

This book provides the most recent studies on interferometry and its applications in science and technology. It is an outline of theoretical and experimental aspects of interferometry and their applications. The book is divided in two sections. The first one is an overview of different interferometry techniques and their general applications, while the second section is devoted to more specific interferometry applications comprising from interferometry for magnetic fusion plasmas to interferometry in wireless networks. The book is an excellent reference of current interferometry applications in science and technology. It offers the opportunity to increase our knowledge about interferometry and encourage researchers in development of new applications.

INTECH
open science | open minds

InTech Europe
University Campus STeP Ri
Slavka Krautzeka 83/A
51000 Rijeka, Croatia
Phone: +385 (51) 770 447
Fax: +385 (51) 686 166
www.intechopen.com

InTech China
Unit 405, Office Block, Hotel Equatorial Shanghai
No.65, Yan An Road (West), Shanghai, 200040, China
中国上海市延安西路65号上海国际贵都大饭店办公楼405单元
Phone: +86-21-62489820
Fax: +86-21-62489821

IntechOpen